Title

Deglacial volcanism and reoxygenation in the aftermath of the Sturtian Snowball Earth.

Journal

Science Advances, 9(36)

Authors

Li, Menghan

Xu, Yilun

Sun, Lilin

et al.

Publication Date

2023-09-08

DOI

10.1126/sciadv.adh9502

Peer reviewed

GEOCHEMISTRY

Deglacial volcanism and reoxygenation in the aftermath of the Sturtian Snowball Earth

Menghan Li[1]*, Yilun Xu[1], Lilin Sun[1], Jiubin Chen[2], Ke Zhang[2], Dandan Li[1], James Farquhar[3], Xiaolin Zhang[1], Ruoyu Sun[2], Francis A. Macdonald[4], Stephen E. Grasby[5], Yong Fu[6], Yanan Shen[1]

The Cryogenian Sturtian and Marinoan Snowball Earth glaciations bracket a nonglacial interval during which Demosponge and green-algal biomarkers first appear. To understand the relationships between environmental perturbations and early animal evolution, we measured sulfur and mercury isotopes from the Datangpo Formation from South China. Hg enrichment with positive Δ^{199}Hg excursion suggests enhanced volcanism, potentially due to depressurization of terrestrial magma chambers during deglaciation. A thick stratigraphic interval of negative $\Delta^{33}S_{py}$ indicates that the nonglacial interlude was characterized by low but rising sulfate levels. Model results reveal a mechanism to produce the Δ^{33}S anomalies down to −0.284‰ through Rayleigh distillation. We propose that extreme temperatures and anoxia contributed to the apparent delay in green algal production in the aftermath of the Sturtian glaciation and the subsequent reoxygenation of the iron-rich and sulfate-depleted ocean paved the way for evolution of animals.

INTRODUCTION

The Cryogenian Period [~720 to 635 million years (Ma) ago] includes the Sturtian and Marinoan Snowball Earth glaciations (*1*), which were separated by a nonglacial interval that preserves biomarker evidence for the rise to dominance of green algae and the first appearance of Demospongiae (*2*, *3*). Ice extended to the equator for millions of years through the 717- to 661-Ma Sturtian glaciation (*4*, *5*) and the >639- to 635-Ma Marinoan glaciation (*1*). During the ~56-Ma-long Sturtian glaciation, iron formations proliferated, requiring anoxic Fe^{2+}-rich and sulfate-depleted deep waters (*6*). A low S:Fe flux to the ocean may have been accomplished by the diminished sulfate input from the continents during the Snowball Earth glaciation and by a lowered S:Fe flux of hydrothermal vent fluids due to the decrease in hydrostatic pressure resulting from glacioeustatic sea-level fall (*7*). Snowball Earth may have provided a bottleneck for some preglacial life-forms but melt ponds on the surface of ice and zones of sublimation were potential nurseries for the diversification of life (*1*).

Deglaciation of the Sturtian Snowball was achieved when atmospheric CO_2 levels and the planetary albedo reached a critical threshold of radiative forcing (*1*). Multicellular animals emerged during or soon after the Sturtian glaciation and expanded to measurable levels during the Cryogenian nonglacial interlude (*2*). It has been proposed that the appearance of animals was a consequence of a surge in phosphorous to the ocean in the aftermath of the Sturtian Snowball Earth, which fueled the dominance of green algae over red algae and provided an increasing energy flow to higher trophic levels (*3*). However, sterane abundance data have revealed a stratigraphic gap of ~200 m in Australia between the end of the Sturtian glaciation and the rise to dominance of green algae (*3*). Post-Sturtian temperatures may have been well above the growth optimum of algae, but within the range of cyanobacterial picoplankton, and thus algae may have only been able to radiate once temperatures fell and nutrient regimes rebounded (*3*). Yet, in the aftermath of the Sturtian glaciation, without an additional increase in CO_2 flux to the atmosphere from enhanced volcanic outgassing, the silicate weathering feedback should have brought temperatures back to a cooler, steady state within 100 thousand years (ka) (*8*). Alternatively, the high productivity of green algae may reflect elevated dissolved iron availability because green algae have higher iron requirements than red algae (*2*, *9*). Uranium isotope and iron speciation data through the Cryogenian nonglacial interlude strata document oxygenation in ferruginous oceans (*10*, *11*). Iron-rich, low-sulfate conditions in the ocean also imply minimal sulfide-rich surface waters, which are toxic to eukaryotes (*2*).

The iron, oxygen, sulfur, and carbon cycles are linked through the burial of organic carbon and pyrite. Thus, multiple sulfur isotopes hold promise for tracking major changes in oxygenation through time. Published δ^{34}S values of pyrite ($\delta^{34}S_{py}$) from the Cryogenian nonglacial interlude show uniformly superheavy values, but their origins are unknown (*12*–*17*). In addition, volcanism emits Hg to the Earth's surface via direct magmatic degassing and by intrusive contact metamorphism with organic-rich rocks (*18*). Elevated Hg contents in sedimentary rocks can thus be used as a proxy for massive volcanisms, which may have triggered global climatic and environmental perturbations (*18*–*24*). To interrogate the relationships between Snowball Earth, volcanism, oxygenation, and life, we analyzed multiple geochemical proxies at a high-resolution, including the mercury (Hg) content, Hg–mass-dependent fractionation (MDF), Hg–mass-independent fractionation (MIF), and multiple S-isotopes of pyrites (table S1).

The Cryogenian Sturtian and Marinoan glacial deposits, and the nonglacial interlude, are well preserved in South China (*25*). Samples of deep-water deposits were collected from drill core ZK102 from Guizhou Province, South China (28°7′54.30″N; 108°53′32.80″) (Fig. 1). The Tiesi'ao Formation is correlated to the

[1]School of Earth and Space Sciences, University of Science and Technology of China, Hefei 230026, China. [2]Institute of Surface-Earth System Science, School of Earth System Science, Tianjin University, Tianjin 300350, China. [3]Department of Geology and ESSIC, University of Maryland, College Park, MD 20742, USA. [4]Department of Earth Science, University of California–Santa Barbara, Santa Barbara, CA 93106, USA. [5]Geological Survey of Canada, Natural Resources Canada, Calgary, Alberta T2L 2A7, Canada. [6]College of Resource and Environmental Engineering, Guizhou University, Guiyang 550012, China.
*Corresponding author. Email: limh@ustc.edu.cn

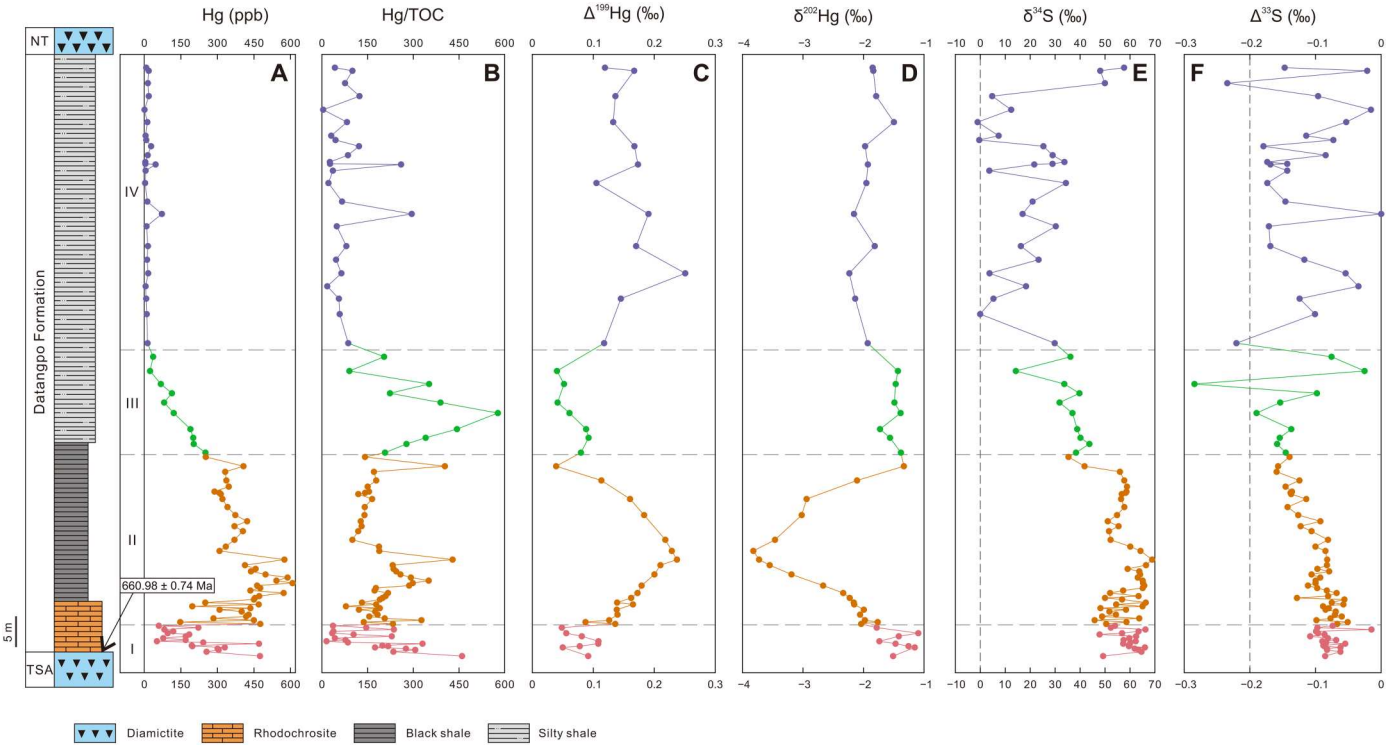

Fig. 1. Hg content, Hg/TOC, Δ^{199}Hg, δ^{202}Hg and δ^{34}S, Δ^{33}S from drill core ZK102. Age from (*5*); ppb, parts per billion.

Sturtian glaciation, which terminated globally at 661 Ma (Fig. 1) (*5*, *26*). The overlying 95.15-m-thick Datangpo Formation consists of a lower rhodochrosite deposit, organic-rich black shale, and interbedded siltstone and shale (Fig. 1). The rhodochrosite deposit was formed during the post-Snowball glacioeustatic transgressive sequence with the maximum flooding surface in the lower half of the black shale unit. In basinal settings, the contact between the Datangpo Formation and the overlying Nantuo Formation glacial deposits appears transitional (*27*). The Nantuo Formation is correlative to the Marinoan glaciation, which terminated globally between 636 and 635 Ma (*28*). The onset of the Marinoan is loosely constrained to be between 652 and 639 Ma (*29*), and the duration of the nonglacial Datangpo Formation is estimated at ~10 Ma (*30*).

RESULTS AND DISCUSSION

Hg content, Hg-MDF, Hg-MIF, and deglacial volcanism

Mercury is emitted to the atmosphere in its reduced gaseous form as Hg^0(g). The long residence time of Hg^0(g) (~1 to 2 years) relative to atmospheric mixing allows a global transport. Deposition of volcanically emitted Hg^0(g) from the atmosphere to the Earth's surface typically occurs by photo-oxidation to oxidized forms (Hg^{2+}), which is soluble and particle reactive with a short residence time of hours to weeks. In the oceans, reactive Hg^{2+} is commonly bound to organic matter (OM) as Hg-OM complexes [e.g., (*31*)]. As such, any potential influences of Hg anomalies due to enhanced organic burial can be minimized by normalizing Hg against total organic carbon (TOC) (*18*, *19*, *32*). In addition, Hg isotopes undergo both Hg-MDF and Hg-MIF (*33*, *34*), which can distinguish Hg sources and transformations during Hg biogeochemical cycles (*20*, *35*–*37*). Hg-MDF, reported as δ^{202}Hg, occurs in numerous biogeochemical processes (*34*). Hg-MIF includes odd-MIF, reported as Δ^{199}Hg or Δ^{201}Hg, and even-MIF, reported as Δ^{200}Hg or Δ^{204}Hg. Even-MIF presumably occurs during photochemical reactions in the upper atmosphere (*38*), and odd-MIF is primarily associated with aqueous photochemical transformations (*39*).

Hg content and isotope data from the Datangpo Formation reveal clear stratigraphic variations, which enable it to be approximately divided into four intervals: I, II, III, and IV (Fig. 1, A to D; the detailed description can be found in the Supplementary Materials: Temporal changes in Hg, Hg/TOC, and Hg isotopes of the Datangpo Formation), described below.

Subaerial volcanism and submarine hydrothermal fields are the primary Hg sources in oceans (*18*, *40*). During the Sturtian Snowball Earth, there was a reduced exchange between the ocean and atmosphere, and Hg in the glacial ocean would have been mostly from hydrothermal discharge [δ^{202}Hg = −1.70 per mil (‰) ± 1.20‰; Δ^{199}Hg = 0.00‰ ± 0.10‰] (*41*). Therefore, the Δ^{199}Hg values (0.08‰ ± 0.02‰) from interval I, which are slightly higher than hydrothermal discharge but lower than the background of marine sediments (~0.12 to 0.25‰ inferred from interval IV), are consistent with Hg isotopic values inherited from the Snowball deepwater.

The elevated Hg contents and Hg/TOC in the lower portion of interval II, enriched by up to 2.5× relative to interval I, are comparable to or slightly lower than the Hg enrichment during Phanerozoic mass extinction events that have been linked to large-scale volcanism (*18*, *19*, *35*–*37*, *42*–*46*). Therefore, the Hg enrichments in interval II provide evidence for the enhanced loading of Hg from volcanism (Fig. 1, A and B). This interpretation is

corroborated by the positive excursion of Δ^{199}Hg (Fig. 1C). Studies on modern Hg cycling show that atmospheric Hg^{2+} species and marine waters/sediments that receive atmospheric Hg^{2+} deposition have exclusively positive Δ^{199}Hg, which is attributed to aqueous or atmospheric photochemical processes (*33*, *47*). Massive subaerial volcanism is expected to eject copious amounts of ash into the atmosphere, which could function as an atmospheric carrier of particle-reactive Hg^{2+} (*36*). In addition, the hydrological cycle was likely enhanced due to rapid global warming following the Snowball Earth, promoting increased rainfall and river discharge, and contributing atmospheric Hg^{2+} to the oceans. Remarkably increased atmospheric Hg^{2+} deposition could account for the positive excursion of Δ^{199}Hg in interval II (Fig. 1C). Therefore, both Hg contents and isotopes provide evidence for an increased atmospheric Hg flux linked to major volcanism in the aftermath of the Sturtian Snowball Earth. The approximate coincidence between the peak Hg content and Hg/TOC, and the peak Δ^{199}Hg values in the lower part of interval II, may be indicative of a peak atmospheric Hg loading from volcanism, and by inference, a peak in enhanced magmatism (Fig. 1, A to C).

To quantitatively estimate the loading of volcanic Hg, we use a simplified box model to simulate the excursions of Hg enrichment and isotope signatures in interval II, with Hg inputs via volcanism and Hg removal via oceanic Hg burial (Fig. 2). The algorithm of the model is based on ordinary differential equations according to Hg mass balance and Hg isotopic mass balance constraints (*33*), which are applied to three coupled reservoirs: atmospheric Hg^0(g), atmospheric Hg^{2+}, and oceanic Hg. The Hg mass and isotope transfers between boxes (reservoirs) are controlled by first-order rate coefficients (k, $year^{-1}$), which are derived from the reservoir masses and fluxes of the well-known modern Hg cycle (*48*, *49*). The initial reservoir sizes are taken from Amos *et al.* (*48*), where atmospheric Hg is speciated as Hg^0(g) (80%) and Hg^{2+} (20%), to investigate the effect resulting from the relative change of atmospheric Hg^0 and Hg^{2+} deposition fluxes (Fig. 2). On the basis of a recent study (*50*), the flux ratio of atmospheric Hg^0 and Hg^{2+} deposition is prescribed as 50% for each (Fig. 2). Before running the model, the ocean reservoir is assumed to be in a steady state (i.e., input = output) in both Hg fluxes and isotopic compositions. According to a recent United Nations Environment Programme Hg assessment report (*51*), the background subaerial volcanic Hg emission flux and submarine hydrothermal flux are assumed to be 150 and 100 Mg $year^{-1}$, respectively (Fig. 2). The hydrothermal discharges are assumed to be −1.7‰ in δ^{202}Hg and 0.00‰ in Δ^{199}Hg, as estimated for the primordial mantle (*41*), and values for subaerial volcanism are assumed to be −0.76‰ in δ^{202}Hg and 0.00‰ in Δ^{199}Hg (Fig. 2) (*52*). According to the mass ratio of atmospheric Hg^0(g)/Hg^{2+} = 80/20%, and the background atmospheric Hg^0(g) isotopic composition (δ^{202}Hg = 0.4‰; Δ^{199}Hg = −0.15‰) (*50*), the background atmospheric Hg^{2+} is resolved as −5.4‰ in δ^{202}Hg and 0.6‰ in Δ^{199}Hg (Fig. 2). This resolved atmospheric $\Delta^{199}Hg^{2+}$ is consistent with modern observations on background rainfall and aerosols, but the resolved $\delta^{202}Hg^{2+}$ is notably lower than the modern rainfall/aerosol observations (*50*), implying complex occurrence of Hg-MDF in nature. We use river discharge in exchange with our modeled ocean to balance the Hg fluxes and isotopic compositions of the modeled ocean (Fig. 2). Given the globally consistent Hg^0(g) and Hg^{2+} isotopic composition observed in the modern atmosphere (*50*), we modify our system to be a simple mixing model for marine Hg isotopic compositions, which greatly reduces the model complexity and possibly uncertainties.

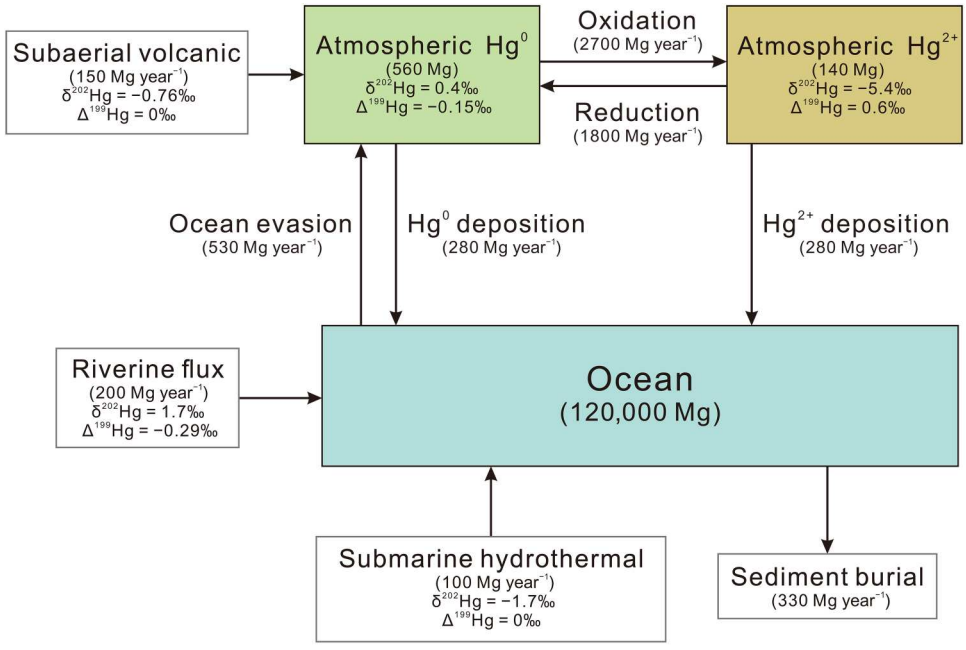

Fig. 2. A simplified ocean-atmosphere Hg cycling box-model. This model is used to simulate the excursions of Hg enrichment and isotope signatures in interval II. The numbers in boxes represent Hg reservoir sizes (Mg), the numbers beside the arrows represent Hg fluxes (Mg $year^{-1}$), which are differentiated by processes identifiers (volcanic Hg emission, hydrothermal Hg discharges, photochemical atmospheric Hg^0 oxidation, photochemical atmospheric Hg^{2+} reduction, atmospheric Hg^0 deposition, atmospheric Hg^{2+} deposition, ocean Hg^0 evasion, riverine flux, and sediment Hg burial).

Starting from the reservoir Hg budgets and Hg isotopic compositions at the steady state, volcanic emissions and associated geochemical perturbations, including changes in atmospheric Hg^0 and Hg^{2+} deposition fluxes, provide constraints on the marine Hg budgets and Hg isotopic changes during interval II (Fig. 3). Our model is time dependent, and we use a nominal 50 ka for the duration of the positive Δ^{199}Hg excursion and 50 ka for the negative Δ^{199}Hg excursion in interval II (Fig. 3). Our model results suggest that a 3.5× increase in volcanic Hg emissions can account for a 2.5× increase in Hg enrichment over time, which is from Hg/TOC = 170 μg kg^{-1} weight % (wt %) in interval I, to peak Hg/TOC = 430 μg kg^{-1} wt % (Fig. 3, A and B). With the return of volcanic Hg emissions to background conditions, Hg enrichment would decrease accordingly (Fig. 3, A and B). However, both δ^{202}Hg and Δ^{199}Hg show a limited variation (Fig. 3, C and D), which cannot explain the substantial changes in δ^{202}Hg and Δ^{199}Hg in interval II (Fig. 1, C and D). Therefore, we explore the change in atmospheric Hg^0 and Hg^{2+} deposition rates to oceans resulting from volcanism, which could potentially account for the temporal variations in δ^{202}Hg and Δ^{199}Hg. We find that a change in rate coefficients associated with atmospheric Hg^{2+} deposition (k_{dep_2}) could change the Δ^{199}Hg and δ^{202}Hg without driving the Hg enrichment. Our model results suggest that an increase in k_{dep_2} by 1.5×, coupled with an increase in volcanic Hg emissions by 3.5×, could explain the positive excursions of Δ^{199}Hg and the Hg enrichment (Fig. 3, E, F, and H). With a return of k_{dep_2} and volcanic Hg emissions to background conditions, the Δ^{199}Hg and Hg enrichment would decrease accordingly (Fig. 3, E, F, and H). However, to reproduce the strong negative δ^{202}Hg seen in interval II, the model needs an increase of k_{dep_2} by 2× (Fig. 3G). In either case, our model suggests that an increase in volcanic Hg emissions and atmospheric Hg^{2+} deposition rate (flux) to the oceans is a key mechanism for explaining the Hg enrichment, the positive excursion of Δ^{199}Hg, and the negative excursion of δ^{202}Hg (Fig. 3).

In interval III, the decreasing Hg contents are accompanied by fluctuating but high Hg/TOC (Fig. 1, A and B). The relatively high Hg/TOC could be a signal of volcanic Hg influx; however, the TOC content decreases sharply from uppermost intervals II to III, and the low TOC could yield a biased Hg/TOC (*18*). Given similar Δ^{199}Hg and δ^{202}Hg values between interval III and the end phase of interval II, we suggest that this interval may record a diminishing volcanic Hg loading (Fig. 1, C and D). The low Hg and Hg/TOC in interval IV indicate little volcanic Hg influx, and the δ^{202}Hg (−1.43 to −2.23‰) and Δ^{199}Hg (0.12 to 0.25‰) in the same interval are consistent with the background Hg isotopic record of modern and ancient marine sediments (Fig. 1, A to D) (*34*).

Enhanced terrestrial magmatism associated with the unloading of ice sheets and decompression melting is expected in the aftermath of Snowball Earth glaciations. This process has been invoked to explain increased volcanic activity in the Quaternary (*53*) and the volcanic activity in the Pacific Ocean known as the "Ring of Fire" during the retreat of the Cordilleran Ice Sheet (*54*), which could contribute to enhanced magmatism on deglacial and glacio-isostatic time scales (i.e., 1 to 100 ka). Although the time scale of deposition for the lower Datangpo Formation is poorly resolved, the position of the peak positive excursion in Δ^{199}Hg and Hg contents near the maximum flooding surface suggests that these signals are associated in time with full global deglaciation, although some sections also show evidence for substantial condensation (*5*). As South China was positioned at mid-latitudes in the Cryogenian (*55*), enhanced volcanism associated with deglaciation could have continued at higher latitudes after the local disappearance of ice. In contrast, the negative excursion of Δ^{199}Hg in upper interval II, and decreased Hg and Hg/TOC, suggest the reduced loading of volcanic-sourced Hg and the decreasing deposition of atmospheric Hg^{2+} to oceans.

Although deglaciation would cause additional loading on mid-ocean ridge magmatism, CO_2 outgassing for mid-ocean ridges versus arcs and plumes is uncertain, and many studies suggest that arc volcanism is the largest flux (*56*). The high background CO_2 needed to initiate deglaciation will be consumed by silicate weathering in <100 ka (*8*), such that the duration of warm temperatures will be a function of the CO_2 flux. The Hg isotopes document a persistent high volcanic flux, and by inference, a high CO_2 flux, through deglaciation to the maximum flooding surface. Although this increased terrestrial volcanic outgassing associated with deglaciation could have contributed to this flux, the duration of enhanced volcanism associated with post–Last Glacial Maximum (LGM) was only ~10 ka (*53*). The duration of post-LGM deglaciation was also ~10 ka, and it is unlikely that Cryogenian snowball deglaciations were much longer because the ice-albedo feedback was stronger due to deglaciation of the tropical ocean. Thus, the time scale for enhanced volcanism associated with depressurization was likely <100 ka and does not fully explain the delay in dominance of green algae to red algae in the sterane records of Australia, more than 200 m above Sturtian glacial deposits (*3*).

Sulfur isotopic anomalies, seawater chemistry changes, and reoxygenation

Like mercury, sulfur can undergo both MDF (S-MDF) and MIF (S-MIF) (*57*–*60*). S-MIF occurs during gaseous-phase photochemical reactions and often produces $\Delta^{33}S > +0.2‰$ or $< -0.2‰$ (*57*). Thermochemical sulfate reduction (TSR) is the only nonatmospheric process that produces large S-MIF from a magnetic isotope effect, yielding a positive Δ^{33}S but without a corresponding Δ^{36}S anomaly (*61*). S-MDF during microbial sulfur cycling usually produces small but measurable Δ^{33}S variations (usually −0.1 to +0.1‰) (*62*). The combination of δ^{34}S and minor but measurable Δ^{33}S provides insights into the evolution of the sulfur cycle and changes in atmospheric and ocean chemistry during Earth's history (*63*–*71*).

The high-resolution S-isotopic data from the rhodochrosite deposit show superheavy $\delta^{34}S_{py}$ ranging from +45.84 to +66.32‰, with $\Delta^{33}S_{py}$ from −0.015 to −0.108‰ (Fig. 1, E and F). Likewise, the overlying black shale of interval II also shows superheavy $\delta^{34}S_{py}$ from +35.36 to +68.90‰, with $\Delta^{33}S_{py}$ from −0.056 to −0.159‰. In contrast, the $\delta^{34}S_{py}$ values in intervals III and IV are relatively light, ranging from −1.07 to +43.73‰, with $\Delta^{33}S_{py}$ from −0.284 to 0.000‰, except for the uppermost three samples, which have $\delta^{34}S_{py}$ from +48.08 to +57.64‰, with $\Delta^{33}S_{py}$ from −0.234 to −0.021‰ (Fig. 1, E and F).

One of the most notable findings from intervals III and IV is the S-isotopic signal with $\Delta^{33}S_{py}$ ranging from −0.284 to −0.221‰, which is beyond the range of typical isotopic fractionations resulting from biogeochemical sulfur cycles (*62*–*64*) (Fig. 1F). Photolysis of sulfur gases and TSR are the only two known mechanisms that produce S-MIF (*57*, *58*, *61*). However, the volcanism evidenced by the Hg content and isotopes in the aftermath of the Sturtian

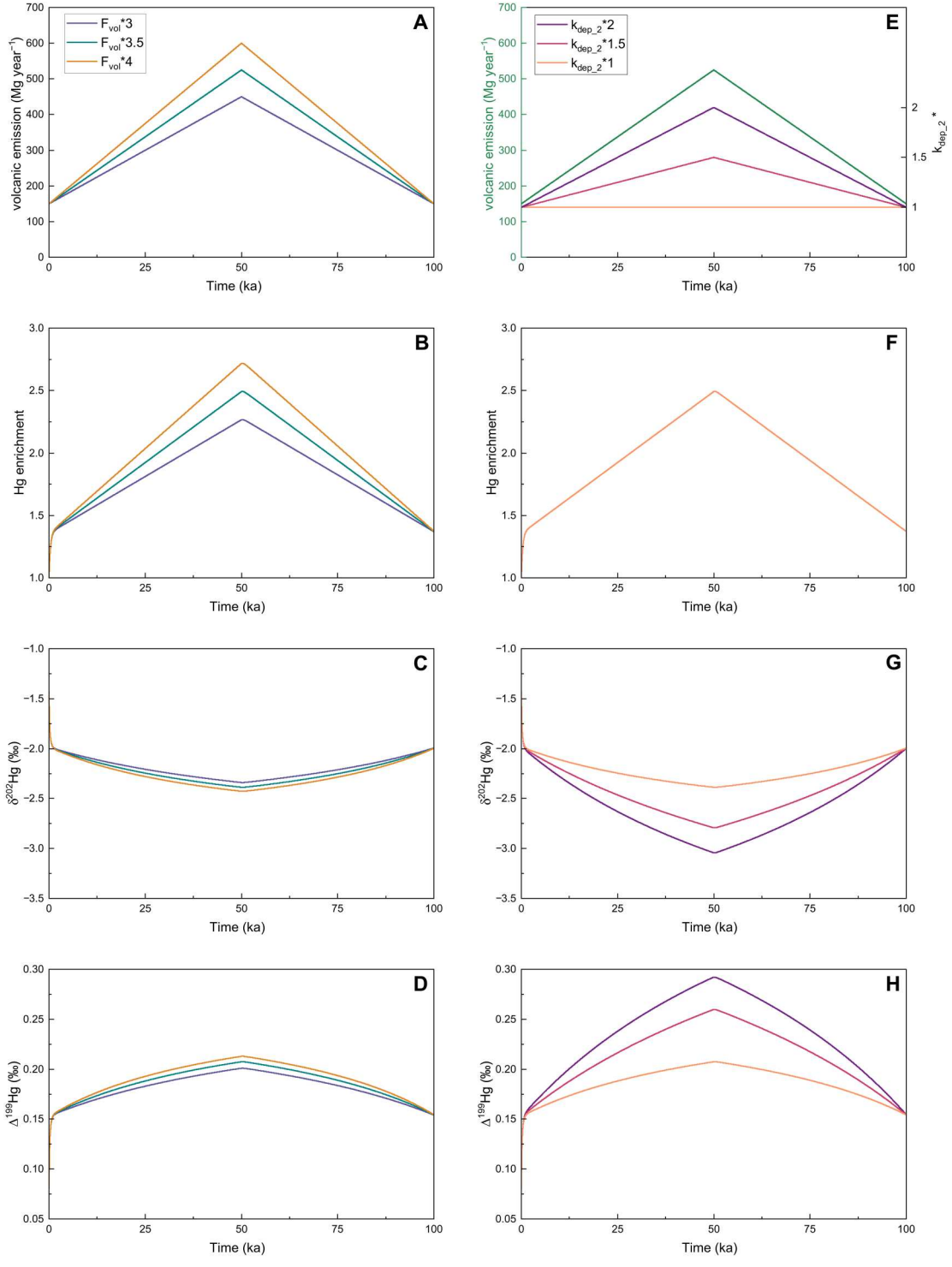

Fig. 3. Simulated Hg enrichment and isotopic excursions in interval II in response to volcanic emissions (F_{vol}) and atmospheric Hg^{2+} deposition rate coefficient (k_{dep_2}). Left: The modeled marine Hg enrichment (**B**), δ^{202}Hg (**C**), and Δ^{199}Hg (**D**) in response to an increase of volcanic Hg emissions by 3 to 4× in the first 50 ka, and a return of volcanic Hg emissions back to the starting condition in the later 50 ka (**A**). Right: The modeled marine Hg enrichment (**F**), δ^{202}Hg (**G**), and Δ^{199}Hg (**H**) in response to an increase of atmospheric Hg^{2+} deposition rate coefficient by 1 to 2× and volcanic Hg emissions by 3.5× in the first 50 ka, and a return of atmospheric Hg^{2+} deposition rate coefficient and volcanic Hg emissions back to the starting condition in the later 50 ka (**E**).

Snowball glaciation occurred before the $\Delta^{33}S_{py}$ anomalies (Fig. 1). Therefore, a stratospheric volcanism model cannot explain the $\Delta^{33}S_{py}$ anomalies. TSR is experimentally demonstrated to produce S-MIF (*61*). However, $\Delta^{33}S$ anomalies resulting from TSR lack corresponding $\Delta^{36}S$ anomalies. In contrast, the $\Delta^{36}S_{py}$ and $\Delta^{33}S_{py}$ are linearly correlated in intervals III and IV (Fig. 4), and therefore, TSR cannot explain the $\Delta^{33}S_{py}$ anomalies from the Datangpo Formation. Present-day Dziani Dzaha Lake, with sulfate concentration, <3 mM, may be a close modern analog, which produces superheavy $\delta^{34}S_{H2S}$ (*72*). However, the superheavy $\delta^{34}S_{H2S}$ from Dziani Dzaha Lake have positive $\Delta^{33}S$ (*72*), and therefore, the Dziani Dzaha Lake model cannot directly be applied to explain the $\delta^{34}S_{py}$ and $\Delta^{33}S_{py}$ from the Datangpo Formation.

Although superheavy $\delta^{34}S_{py}$ in the rhodochrosite deposit was reported more than 30 years ago (*15*), our study reveals systematic "light" $\delta^{34}S$ values down to −1.07‰ overlying the superheavy $\delta^{34}S$ strata (Fig. 1E). The superheavy $\delta^{34}S_{py}$ from the nonglacial interlude has been interpreted to result from microbial sulfate reduction (MSR) under low-sulfate conditions, TSR, or sulfide methylation (*12*–*15*, *73*). However, previous models are based on $\delta^{34}S_{py}$ data only and do not address the $\Delta^{33}S_{py}$ and overlying light $\delta^{34}S_{py}$.

To understand the environmental significance of the S-isotopic data from the Datangpo Formation, we present modeling work for MSR and a Rayleigh distillation process that are based on the MSR model of Brunner and Bernasconi (*74*), Farquhar *et al.* (*75*), and Zhang *et al.* (*76*), and the Rayleigh model of Scott *et al.* (*77*). Our updated sulfur cycle models represent all possible isotopic fractionation pathways and provide a framework for interpreting the S-isotopic data from the Datangpo Formation.

The total sulfur isotope fractionation ($^{34}\alpha_{net}$ and $^{33}\alpha_{net}$) during MSR is generally modeled as a superposition of the reversibility of individual enzymatically catalyzed steps, with any corresponding isotope fractionation occurring at each step (*74*–*76*). Instead of assigning a fixed value to each enzymatically catalyzed step in MSR, as was previously done (*74*–*76*), the magnitude of fractionations at each step in our updated MSR model is the function of equilibrium fractionation, kinetic fractionation, and the reversibility of individual enzymatically catalyzed steps (*67*). Accordingly, the $\delta^{34}S$ and $\Delta^{33}S$ of the product sulfide can be calculated using our MSR model for a given isotopic composition of the starting sulfate (the detailed calculation can be found in the Supplementary Materials: MSR model; fig. S1).

In the previous Rayleigh model, a linear correlation between $^{33}\lambda_{net}$ and $^{34}\alpha_{net}$ [expressed as $1000 \times \ln(^{34}\alpha_{net})$] is assumed on the basis of the isotopic data from the open-system MSR experiments, and accordingly the $^{33}\alpha_{net}$ values are calculated using $^{33}\lambda_{net}$ and $^{34}\alpha_{net}$ (*77*). However, culture experiments and theoretical work have shown that the specific value of $^{34}\alpha_{net}$ during MSR could correspond to a series of $^{33}\lambda_{net}$ values rather than to a single value (*78*). In our Rayleigh model, the fractionation factor describing isotope partitioning between the product sulfide and reactant sulfate in the Rayleigh fractionation equations from Scott *et al.* (*77*) are substituted by $^{34}\alpha_{net}$ and $^{33}\alpha_{net}$ values, which are calculated using our revised MSR model. In this way, the assumption by the previous Rayleigh model that $^{33}\lambda_{net}$ varies linearly with $1000 \times \ln(^{34}\alpha_{net})$ can be avoided. Therefore, for a given f (f = unconsumed sulfate/starting sulfate and varies from 1 to 0), the $\delta^{34}S$ and $\Delta^{33}S$ of both sulfate and sulfide produced during distillation processes can be modeled (the detailed calculation can be found in the Supplementary Materials: A Rayleigh distillation model).

During the ~57-Ma-long Sturtian Snowball glaciation, when oceans had few sulfur inputs from the continents, the seawater sulfate in the glacial ocean would be largely drawn down to extremely low levels by distillation processes. Thus, the evolution of $\Delta^{33}S$ for seawater sulfate can be modeled using our Rayleigh model. For example, starting with seawater sulfate with $\delta^{34}S$ = +30‰ and $\Delta^{33}S$ = 0‰, our model results suggest that the $\Delta^{33}S$ of residual sulfate = −0.20‰, when more than ~90% of sulfate is reduced (i.e., $f \leq 0.1$), which may be the approximate limit of S-MDF due to the conservation of mass in the sulfur cycle (Fig. 5). Note that the change in $\delta^{34}S$ of the starting seawater sulfate does not change the trajectory of $\Delta^{33}S$ for the residual sulfate. It is unlikely that photochemical reactions known to produce S-MIF could have a substantial impact on the $\Delta^{33}S$ of seawater sulfate in an ice-covered ocean. Therefore, we suggest that the seawater sulfate in the aftermath of the Sturtian Snowball had a notable negative $\Delta^{33}S$ (~−0.20‰). This is consistent with the previous estimate of $\Delta^{33}S$

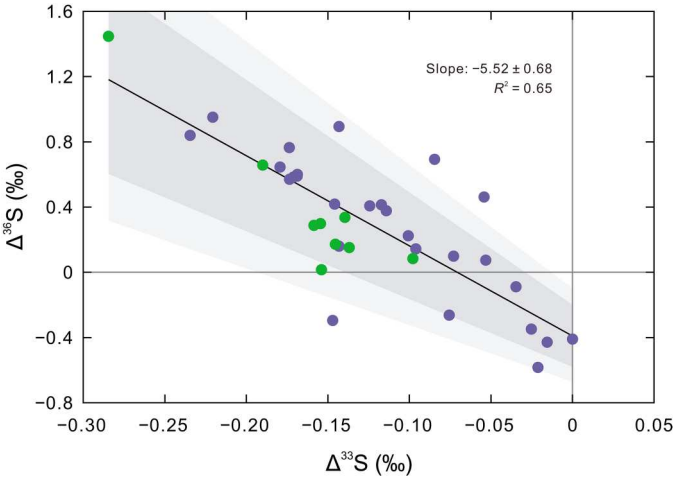

Fig. 4. Cross plot of $\Delta^{33}S$ and $\Delta^{36}S$ for intervals III and IV in drill core ZK102. The black line shows linear regression slope, and the dark gray and light gray areas show 2σ and 3σ confidence intervals, respectively.

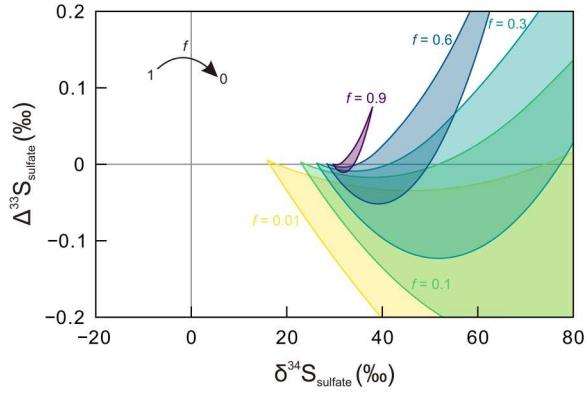

Fig. 5. $\delta^{34}S$ and $\Delta^{33}S$ evolution of sulfate during a Rayleigh distillation process. Starting sulfate $\Delta^{33}S$ = 0‰ and $\delta^{34}S$ = +30‰.

for the pre–Marinoan Neoproterozoic seawater sulfate, which varies between −0.1‰ and −0.2‰ (*16*).

The $\delta^{34}S$ values of anhydrite between the Sturtian and Marinoan Snowballs, a proxy for seawater sulfate, range from +25.8 to +27.0‰, with an average of +26.3‰ (*12*). The evolution of sulfide produced by MSR and the Rayleigh distillation processes is modeled using a starting seawater sulfate with $\delta^{34}S$ = +30‰ and $\Delta^{33}S$ = −0.2‰ (Fig. 6). Evidently, a Rayleigh distillation process alone adequately explains the superheavy $\delta^{34}S_{py}$ and negative $\Delta^{33}S_{py}$ in intervals I and II under conditions of ~70 to 90% of sulfate being reduced (i.e., f = 0.3 to 0.1) (Fig. 6), which suggests that sulfate consumption outpaced sulfate inputs and that sulfate concentrations remained extremely low. However, under such low-sulfate conditions, there is little isotopic evidence showing that sulfate aerosols originating from the volcanism during interval II have affected sulfur cycling in the post-Sturtian oceans. Volcanic eruptions are known to have played a critical role in climate changes and oceanic anoxia, and the largest climate impacts occur when volcanic eruptions reach the stratosphere (*79*). The sulfur ejected from stratospheric volcanic eruptions will be exposed to ultraviolet radiation at or above the ozone layer, which induces an S-MIF as observed in polar snow, ice cores, and rock record (*60*, *80*–*82*). In contrast, volcanogenic sulfur emitted from tropospheric eruptions is rapidly oxidized to sulfate which is washed out of the atmosphere in the order of weeks (*79*, *83*). Therefore, the large deposition of stratospheric sulfate aerosols into a sulfate-poor ocean could elevate the sulfate levels and have affected the $\Delta^{33}S$ of seawater sulfate as well as biogenic pyrite. However, the pyrites from intervals I and II have nearly identical $\Delta^{33}S$ and $\delta^{34}S$ compositions, showing little isotopic consequence of stratospheric volcanism during interval II. Therefore, we suggest that the volcanism evidenced by the Hg content and isotopes during interval II may represent tropospheric eruptions that may have contributed to oceanic anoxia. Alternatively, deposition of the sulfate aerosols from stratospheric volcanism was too little to affect sulfur cycling in the post-Sturtian oceans.

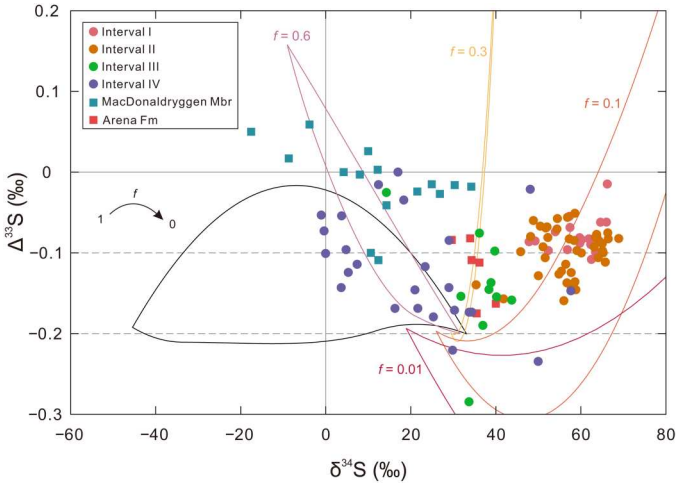

Fig. 6. Cross plot of $\delta^{34}S$ and $\Delta^{33}S$ in drill core ZK102 and correlative strata of the MacDonaldryggen Member in Svalbard and the Arena Formation in East Greenland. S-isotopic data from the MacDonaldryggen Member and the Arena Formation are from (*16*). The model field for sulfate reduction (black outlined field) represents the field of all possible fractionations, and the Rayleigh-colored field indicates $\delta^{34}S$ and $\Delta^{33}S$ evolution from f = 1 to 0.

The $\delta^{34}S_{py}$ and $\Delta^{33}S_{py}$ from interval III and part of interval IV are also interpreted by the Rayleigh model (Fig. 6). Accordingly, the $\Delta^{33}S_{py}$ anomalies ranging from −0.221 to −0.284‰ may have resulted from a Rayleigh distillation process during which sulfate was almost completely reduced (i.e., $f \leq 0.01$) (Fig. 6), rather than photolysis of sulfur gases or TSR. We suggest that the $\Delta^{33}S_{py}$ anomalies from the Datangpo Formation represent a pathway for producing $\Delta^{33}S_{py}$ anomalies in an ice-free ocean that inherited the S-isotopic signal of the Sturtian glacial seawater. The $\delta^{34}S_{py}$ and $\Delta^{33}S_{py}$ from intervals III and IV in the Rayleigh field suggest ~40 to 90% of sulfate being reduced (i.e., f = 0.6 to 0.1), which are statistically lower than intervals I and II (Fig. 6). However, unlike intervals I and II, many of the $\delta^{34}S_{py}$ and $\Delta^{33}S_{py}$ values in interval IV may be explained by open-system MSR, suggesting nonlimiting sulfate conditions (Fig. 6).

The temporal changes in $\delta^{34}S_{py}$ from superheavy to relatively light values suggest that sulfate concentrations increased from intervals I and II to intervals III and IV. An increase in sulfate concentrations, and by inference, an increase of the oxygen content of the ocean and atmosphere, is consistent with the post-Sturtian oxygenation of the deep ocean (*10*, *11*, *55*). The return to the superheavy $\delta^{34}S$ in the uppermost Datangpo Formation is consistent with a decrease in sulfate levels before the onset of the Marinoan Snowball Earth glaciation, but with only three data points and unknown time missing at the base of the Nantuo Formation, interpretation of these outliers remains speculative. It was estimated that sulfate concentrations were <1 mM before the onset of the Nantuo glaciation based on the $\delta^{34}S$ data from the top Datangpo Formation (*84*). Using the same diagenetic model, our $\delta^{34}S$ data suggest sulfate concentrations of ~2 to 4 mM during intervals III and IV, which are substantially lower than the modern ocean value of ~28 mM.

Our interpretation of $\delta^{34}S_{py}$ from the Datangpo Formation is strengthened by the S-isotopic data from correlative strata of the MacDonaldryggen Member in Svalbard and the Arena Formation in East Greenland, both of which were deposited in the aftermath of the Sturtian Snowball glaciation (*16*). For both units, positive $\delta^{34}S_{py}$ with negative $\Delta^{33}S_{py}$ can be interpreted with the Rayleigh model (Fig. 6). Like the Datangpo Formation, the $\delta^{34}S_{py}$ becomes lighter from the lower to upper MacDonaldryggen Member, suggesting an increase in sulfate levels. In addition, three samples in the upper MacDonaldryggen Member with negative $\delta^{34}S_{py}$ and positive $\Delta^{33}S_{py}$, also resulting from nonlimiting sulfate conditions, reflect a second-order variability and can be explained by an MSR model with starting $\Delta^{33}S$ = −0.12‰ for seawater sulfate (Fig. 6). In summary, the similar negative $\Delta^{33}S_{py}$ and positive $\delta^{34}S_{py}$ values from the Datangpo Formation in South China, the Arena Formation in East Greenland, and the MacDonaldryggen Member in Svalbard suggest that the Cryogenian nonglacial interlude was characterized by low but increasing sulfate levels.

The rise of animals in the aftermath of the Sturtian snowball earth

Our independent Hg and S proxies provide a window into the environmental consequences of the Sturtian Snowball Earth and their potential link to early animal evolution (Fig. 7). It was proposed that high temperatures in the aftermath of the Sturtian glaciation delayed the dominance of green algae (*3*), but an additional CO_2 flux to the atmosphere is required for high temperatures to persist. The Hg content and isotopes provide evidence for enhanced

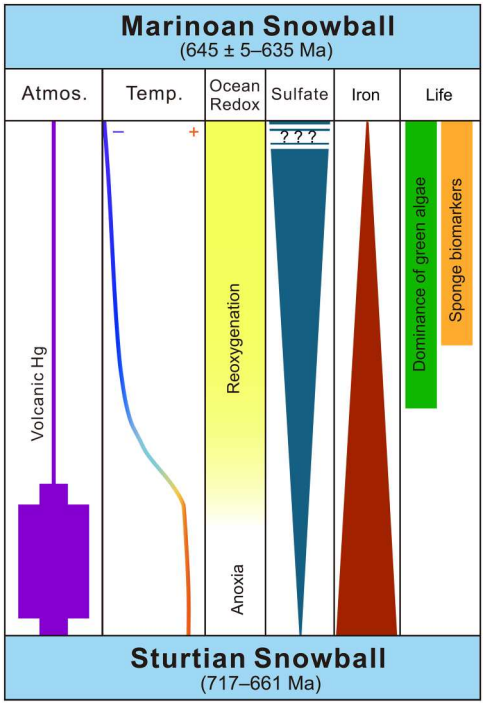

Fig. 7. Schematic illustration of volcanic activity, temperature, ocean redox state, sulfate levels, iron, and early metazoan evolution during the Cryogenian Period. Ocean redox state from (*11*); Early metazoan evolution from (*2*, *3*); Atmos, atmosphere; Temp, temperature.

terrestrial volcanism in the aftermath of the Sturtian Snowball Earth (Fig. 7). We propose that deglaciation depressurized terrestrial volcanic centers driving enhanced eruptions and outgassing, contributing to high temperatures, anoxia, and environmental stress, but the time scale of this enhanced flux of <100 ka is too short to explain the stratigraphic gap of green algae and animals for >200 m after the Sturtian glaciation (*3*).

The subsequent dominance of green algae and appearance of animals have been attributed to either a surge of nutrients supplied by the Sturtian deglaciation (*3*) or elevated dissolved iron and low-sulfate conditions (*2*). Phosphorous delivery from the continents to the oceans is tightly linked to silicate weathering. Consequently, after the excess CO_2 from the syn-Snowball buildup and deglacial volcanism was consumed, phosphorous delivery to the oceans should also have declined, and thus it is not clear how this bloom was sustained. Alternatively, our data are more consistent with the importance of Fe-S-O cycles, and the importance of persistent anoxia as a limiting factor for the rise of animals. After the return to iron formation deposition through the Sturtian glaciation, the oceans remained ferruginous through the Cryogenian nonglacial interlude (*10*). The negative $\Delta^{33}S_{py}$ for 15 ± 5 Ma indicates that during the nonglacial interlude the superheavy $\delta^{34}S_{py}$ and $\Delta^{33}S_{py}$ anomalies were imprinted on the S-isotopic composition of the Sturtian glacial seawater. The identification of relatively light $\delta^{34}S_{py}$ coupled with negative $\Delta^{33}S$ provides evidence for low sulfate and progressive reoxygenation in the aftermath of the Sturtian Snowball Earth (Fig. 7). The rise of green algae under iron-rich, low-sulfate conditions would have provided the required trophic web for eukaryotes without toxic sulfide-rich shallow waters (Fig. 7) (*2*). We propose that extreme high temperatures and anoxia contributed to the apparent delay in green algal productivity in the aftermath the Sturtian glaciation, and that the subsequent oxygenation in high-Fe and low-sulfate oceans paved the way for evolution of early animals.

MATERIALS AND METHODS

Hg content analysis

Hg content and isotopes were analyzed at the Tianjin University, China following published methods (*43*, *85*). Powdered ~5-g samples were step-heated in a dual-stage combustion system to liberate Hg from the sediment matrix. This system consists primarily of a combustion furnace programmed to raise the temperature from ambient to 950°C and a decomposition furnace with a constant temperature of 1000°C. The Hg species were converted to Hg^0 and transported by Hg-free oxygen gas with a flow rate of 20 ml/min and then quantitatively trapped as Hg^{2+} by bubbling through a solution of 50% HNO_3-HCl (v/v = 2:1) mixture. Following preconcentration, aqueous Hg^{2+} was reduced to Hg^0 by reaction with $SnCl_2$. The Hg^0 product was purged from the solution by a Hg-free nitrogen flow onto a gold trap, and then the Hg concentrations were determined using a cold-vapor atomic fluorescence spectrophotometry analyzer. Reproducibility of duplicate analyses of samples was within 5%, and a certified reference material (GBW07405) that was analyzed simultaneously, showing Hg recovery of 99 ± 6%, consistent with that of Huang *et al.* (*85*).

Hg isotopic analyses

Hg isotopic compositions were measured using a Nu-Plasma multicollector inductively coupled plasma mass spectrometer (MC-ICP-MS), following methods outlined by Huang *et al.* (*85*). The instrumental mass bias was corrected by an internal thallium (Tl) standard (NIST SRM 997) and standard-sample bracketing technique using a NIST SRM 3133 solution with concentration and matrix matched to sample. The Hg and Tl were introduced into the mass spectrometer by a continuous flow cold-vapor generation system and an Aridus II desolvation unit (CETAC Technologies, USA), respectively. Before each sample and standard analysis, the instrumental baseline was determined by defocusing.

The MDF of Hg isotopes is reported in delta notation (δ) as per mill (‰) relative to the NIST SRM 3133 Hg standard:

$$\delta^{202}Hg = [(^{202}Hg/^{198}Hg)_{sample}/(^{202}Hg/^{198}Hg)_{NIST\ SRM\ 3133} - 1] \times 1000$$

The MIF of Hg isotopes is expressed using the capital delta notation (Δ), which represents the deviation of the measured isotopic composition from the theoretical composition predicted by the MDF law:

$$\Delta^{199}Hg = \delta^{199}Hg - 0.252 \times \delta^{202}Hg$$

The quality of the Hg isotopic data was assessed by repeated measurements of a laboratory standard (UM-Almaden), which yielded an average Hg isotopic composition and external reproducibility of −0.58‰ ± 0.07‰, −0.01‰ ± 0.06‰, and −0.01‰ ± 0.08‰ for $\delta^{202}Hg$, $\Delta^{199}Hg$, and $\Delta^{201}Hg$, respectively (2SD, n = 5), consistent with results reported in previous studies (*38*, *39*, *43*, *85*).

Sulfur isotopic analyses

Multiple S-isotope measurements were performed at Biogeochemistry Laboratory, University of Science and Technology of China and the Stable Isotope Laboratory of the University of Maryland, following published procedures (*66*) (sample 1315.3 m was analyzed at the University of Maryland and all other samples were analyzed at the University of Science and Technology of China). Dried ~3-mg Ag_2S was weighed and wrapped in a ~1-cm^2 piece of aluminum foil and then loaded in a nickel reaction vessel where Ag_2S was converted to sulfur hexafluoride (SF_6) via reaction with 10× excess F_2 gas at ~250°C overnight. The resulting SF_6 was isolated in a liquid-nitrogen-cooled trap from the residual F_2 that was passivated through a column of hot potassium bromide (KBr). The SF_6 was subsequently distilled at ~−110°C to remove condensable contaminants and then further purified with a gas chromatograph equipped with a composite molecular sieve 5-Å lead/Haysep-Q column, operating isothermally at 50°C, with a 20 ml/min helium flow rate. The SF_6 peak was monitored with a thermal conductivity detector and frozen into two liquid-nitrogen-cooled traps and then transferred to the manifold. S-isotopic measurements of clean SF_6 were conducted using a Thermo Finnigan MAT 253 dual-inlet gas source mass spectrometer where the ion beams at mass/charge ratio = 127, 128, 129, and 131 were detected simultaneously. S-isotope data are reported in per mill (‰) relative to the Vienna Canyon Diablo Troilite (V-CDT) standard using the conventional delta notation

$$\delta^{33}S = [(^{33}S/^{32}S)_{sample}/(^{33}S/^{32}S)_{V-CDT} - 1] \times 1000$$

$$\delta^{34}S = [(^{34}S/^{32}S)_{sample}/(^{34}S/^{32}S)_{V-CDT} - 1] \times 1000$$

$$\Delta^{33}S = \delta^{33}S - [(1 + \delta^{34}S/1000)^{0.515} - 1] \times 1000$$

The capital delta notation is defined with exponents of 0.515 and 1.90 to approximate the deviation from single step low-temperature equilibrium exchange reactions (*86*, *87*). All data are reported relative to V-CDT, with an accepted IAEA S-1 composition of $\delta^{33}S$ = −0.06‰, $\delta^{34}S$ = −0.30‰, and $\delta^{36}S$ = −1.26‰. The analytical reproducibility for $\delta^{34}S$, $\Delta^{33}S$, and $\Delta^{36}S$ is better than ±0.1‰, ± 0.01‰, and ± 0.2‰, respectively, as determined by replicate analyses of IAEA S-1.

TOC analysis

Approximately 1 g of whole rock powder was weighed and then acidified with 6 M HCl (*43*). Insoluble residues were rinsed with deionized H_2O, centrifuged, and decanted several times to completely remove the HCl, and then oven-dried at ~50°C. TOC content was measured by elemental analyzer. The analytical uncertainty of TOC is within ±4% of reported values, based on reproducibility and repeats of standard run after every six sample analyses.

Supplementary Materials

This PDF file includes:

Fig. S1
Legend for table S1
References

Other Supplementary Material for this manuscript includes the following:

Table S1

REFERENCES AND NOTES

1. P. F. Hoffman, D. S. Abbot, Y. Ashkenazy, D. I. Benn, J. J. Brocks, P. A. Cohen, G. M. Cox, J. R. Creveling, Y. Donnadieu, D. H. Erwin, I. J. Fairchild, D. Ferreira, J. C. Goodman, G. P. Halverson, M. F. Jansen, G. Le Hir, G. D. Love, F. A. Macdonald, A. C. Maloof, C. A. Partin, G. Ramstein, B. E. J. Rose, C. V. Rose, P. M. Sadler, E. Tziperman, A. Voigt, S. G. Warren, Snowball Earth climate dynamics and Cryogenian geology-geobiology. *Sci. Adv.* **3**, e1600983 (2017).
2. G. D. Love, E. Grosjean, C. Stalvies, D. A. Fike, J. P. Grotzinger, A. S. Bradley, A. E. Kelly, M. Bhatia, W. Meredith, C. E. Snape, S. A. Bowring, D. J. Condon, R. E. Summons, Fossil steroids record the appearance of Demospongiae during the Cryogenian period. *Nature* **457**, 718–721 (2009).
3. J. J. Brocks, A. J. M. Jarrett, E. Sirantoine, C. Hallmann, Y. Hoshino, T. Liyanage, The rise of algae in Cryogenian oceans and the emergence of animals. *Nature* **548**, 578–581 (2017).
4. F. A. Macdonald, M. D. Schmitz, J. L. Crowley, C. F. Roots, D. S. Jones, A. C. Maloof, J. V. Strauss, P. A. Cohen, D. T. Johnston, D. P. Schrag, Calibrating the cryogenian. *Science* **327**, 1241–1243 (2010).
5. A. D. Rooney, C. Yang, D. J. Condon, M. Zhu, F. A. Macdonald, U-Pb and Re-Os geochronology tracks stratigraphic condensation in the Sturtian snowball Earth aftermath. *Geology* **48**, 625–629 (2020).
6. G. M. Cox, G. P. Halverson, W. G. Minarik, D. P. Le Heron, F. A. Macdonald, E. J. Bellefroid, J. V. Strauss, Neoproterozoic iron formation: An evaluation of its temporal, environmental and tectonic significance. *Chem. Geol.* **362**, 232–249 (2013).
7. L. R. Kump, W. E. Seyfried Jr., Hydrothermal Fe fluxes during the Precambrian: Effect of low oceanic sulfate concentrations and low hydrostatic pressure on the composition of black smokers. *Earth Planet. Sci. Lett.* **235**, 654–662 (2005).
8. J. A. Higgins, D. P. Schrag, Aftermath of a snowball Earth. *Geochem. Geophys. Geosyst.* **4**, 1028 (2003).
9. P. G. Falkowski, M. E. Katz, A. H. Knoll, A. Quigg, J. A. Raven, O. Schofield, F. J. R. Taylor, The evolution of modern eukaryotic phytoplankton. *Science* **305**, 354–360 (2004).
10. E. A. Sperling, C. Carbone, J. V. Strauss, D. T. Johnston, G. M. Narbonne, F. A. Macdonald, Oxygen, facies, and secular controls on the appearance of Cryogenian and Ediacaran body and trace fossils in the Mackenzie Mountains of northwestern Canada. *Geol. Soc. Am. Bull.* **128**, 558–575 (2016).
11. K. V. Lau, F. A. Macdonald, K. Maher, J. L. Payne, Uranium isotope evidence for temporary ocean oxygenation in the aftermath of the Sturtian Snowball Earth. *Earth Planet. Sci. Lett.* **458**, 282–292 (2017).
12. P. Gorjan, J. J. Veevers, M. R. Walter, Neoproterozoic sulfur-isotope variation in Australia and global implications. *Precambrian Res.* **100**, 151–179 (2000).
13. P. Gorjan, M. R. Walter, R. Swart, Global Neoproterozoic (Sturtian) post-glacial sulfide-sulfur isotope anomaly recognised in Namibia. *J. African Earth Sci.* **36**, 89–98 (2003).
14. X. Lang, Z. Zhao, H. Ma, K. Huang, S. Li, C. Zhou, S. Xiao, Y. Peng, Y. Liu, W. Tang, B. Shen, Cracking the superheavy pyrite enigma: Possible roles of volatile organosulfur compound emission. *Natl. Sci. Rev.* **8**, nwab034 (2021).
15. H. Cui, K. Kitajima, M. J. Spicuzza, J. H. Fournelle, A. Denny, A. Ishida, F. Zhang, J. W. Valley, Questioning the biogenicity of Neoproterozoic superheavy pyrite by SIMS. *Am. Mineral.* **103**, 1362–1400 (2018).
16. M. Kunzmann, T. H. Bui, P. W. Crockford, G. P. Halverson, C. Scott, T. W. Lyons, B. A. Wing, Bacterial sulfur disproportionation constrains timing of Neoproterozoic oxygenation. *Geology* **45**, 207–210 (2017).
17. E. L. Scheller, A. J. Dickson, D. E. Canfield, C. Korte, K. K. Kristiansen, T. W. Dahl, Ocean redox conditions between the snowballs – Geochemical constraints from Arena Formation, East Greenland. *Precambrian Res.* **319**, 173–186 (2018).
18. S. E. Grasby, T. R. Them, Z. Chen, R. Yin, O. H. Ardakani, Mercury as a proxy for volcanic emissions in the geologic record. *Earth Sci. Rev.* **196**, 102880 (2019).
19. H. Sanei, S. E. Grasby, B. Beauchamp, Latest Permian mercury anomalies. *Geology* **40**, 63–66 (2012).
20. J. Meixnerová, J. D. Blum, M. W. Johnson, E. E. Stüeken, M. A. Kipp, A. D. Anbar, R. Buick, Mercury abundance and isotopic composition indicate subaerial volcanism prior to the end-Archean "whiff" of oxygen. *Proc. Natl. Acad. Sci. U.S.A.* **118**, e2107511118 (2021).
21. L. M. E. Percival, M. Ruhl, S. P. Hesselbo, H. C. Jenkyns, T. A. Mather, J. H. Whiteside, Mercury evidence for pulsed volcanism during the end-Triassic mass extinction. *Proc. Natl. Acad. Sci. U.S.A.* **114**, 7929–7934 (2017).
22. A. L. Zerkle, R. Yin, C. Chen, X. Li, G. J. Izon, S. E. Grasby, Anomalous fractionation of mercury isotopes in the Late Archean atmosphere. *Nat. Commun.* **11**, 1709 (2020).

23. A. L. Zerkle, M. W. Claire, T. Di Rocco, N. V. Grassineau, E. G. Nisbet, R. Sun, R. Yin, Sulfur and mercury MIF suggest volcanic contributions to Earth's atmosphere at 2.7 Ga. *Geochem. Perspect. Lett.* **18**, 48–52 (2021).
24. M. Ruhl, S. P. Hesselbo, H. C. Jenkyns, W. Xu, R. L. Silva, K. J. Matthews, T. A. Mather, C. Mac Niocaill, J. B. Riding, Reduced plate motion controlled timing of Early Jurassic Karoo-Ferrar large igneous province volcanism. *Sci. Adv.* **8**, eabo0866 (2022).
25. H. Liu, *The Sinian System in China* (Science Press, 1991), pp. 388.
26. C. Zhou, M. H. Huyskens, X. Lang, S. Xiao, Q.-Z. Yin, Calibrating the terminations of Cryogenian global glaciations. *Geology* **47**, 251–254 (2019).
27. X. Bao, S. Zhang, G. Jiang, H. Wu, H. Li, X. Wang, Z. An, T. Yang, Cyclostratigraphic constraints on the duration of the Datangpo Formation and the onset age of the Nantuo (Marinoan) glaciation in South China. *Earth Planet. Sci. Lett.* **483**, 52–63 (2018).
28. D. Condon, M. Zhu, S. A. Bowring, W. Wang, A. Yang, Y. Jin, U–Pb ages from the Neoproterozoic Doushantuo Formation, China. *Science* **308**, 95–98 (2005).
29. L. L. Nelson, E. F. Smith, E. B. Hodgin, J. L. Crowley, M. D. Schmitz, F. A. Macdonald, Geochronological constraints on Neoproterozoic rifting and onset of the Marinoan glaciation from the Kingston Peak Formation in Death Valley, California (USA). *Geology* **48**, 1083–1087 (2020).
30. P. Liu, X. Li, S. Chen, Z. Lan, B. Yang, X. Shang, C. Yin, New SIMS U–Pb zircon age and its constraint on the beginning of the Nantuo glaciation. *Sci. Bull.* **60**, 958–963 (2015).
31. W. F. Fitzgerald, C. H. Lamborg, C. R. Hammerschmidt, Marine biogeochemical cycling of mercury. *Chem. Rev.* **107**, 641–662 (2007).
32. S. E. Grasby, H. Sanei, B. Beauchamp, Z. Chen, Mercury deposition through the Permo-Triassic Biotic Crisis. *Chem. Geol.* **351**, 209–216 (2013).
33. R. Sun, M. Jiskra, H. M. Amos, Y. Zhang, E. M. Sunderland, J. E. Sonke, Modelling the mercury stable isotope distribution of Earth surface reservoirs: Implications for global Hg cycling. *Geochim. Cosmochim. Acta* **246**, 156–173 (2019).
34. J. D. Blum, L. S. Sherman, M. W. Johnson, Mercury isotopes in earth and environmental sciences. *Annu. Rev. Earth Planet. Sci.* **42**, 249–269 (2014).
35. A. M. Thibodeau, K. Ritterbush, J. A. Yager, A. J. West, Y. Ibarra, D. J. Bottjer, W. M. Berelson, B. A. Bergquist, F. A. Corsetti, Mercury anomalies and the timing of biotic recovery following the end-Triassic mass extinction. *Nat. Commun.* **7**, 11147 (2016).
36. S. E. Grasby, W. Shen, R. Yin, J. D. Gleason, J. D. Blum, R. F. Lepak, J. P. Hurley, B. Beauchamp, Isotopic signatures of mercury contamination in latest Permian oceans. *Geology* **45**, 55–58 (2017).
37. R. Sun, Y. Liu, J. E. Sonke, F. Zhang, Y. Zhao, Y. Zhang, J. Chen, C.-Q. Liu, S. Shen, A. D. Anbar, W. Zheng, Mercury isotope evidence for marine photic zone euxinia across the end-Permian mass extinction. *Commun. Earth Environ.* **4**, 159 (2023).
38. J. Chen, H. Hintelmann, X. Feng, B. Dimock, Unusual fractionation of both odd and even mercury isotopes in precipitation from Peterborough, ON, Canada. *Geochim. Cosmochim. Acta* **90**, 33–46 (2012).
39. B. A. Bergquist, J. D. Blum, Mass-dependent and -independent fractionation of Hg isotopes by photoreduction in aquatic systems. *Science* **318**, 417–420 (2007).
40. J. Yuan, Y. Liu, S. Chen, X. Peng, Y. Li, S. Li, R. Zhang, W. Zheng, J. Chen, R. Sun, L.-E. Heimbürger-Boavida, Mercury isotopes in deep-sea epibenthic biota suggest limited Hg transfer from photosynthetic to chemosynthetic food webs. *Environ. Sci. Technol.* **57**, 6550–6562 (2023).
41. F. Moynier, M. G. Jackson, K. Zhang, H. Cai, S. A. Halldorsson, R. Pik, J. M. D. Day, J. Chen, The mercury isotopic composition of Earth's mantle and the use of mass independently fractionated Hg to test for recycled crust. *Geophys. Res. Lett.* **48**, e2021GL094301 (2021).
42. Q. Gong, X. Wang, L. Zhao, S. E. Grasby, Z.-Q. Chen, L. Zhang, Y. Li, L. Cao, Z. Li, Mercury spikes suggest volcanic driver of the Ordovician-Silurian mass extinction. *Sci. Rep.* **7**, 5304 (2017).
43. D. Hu, M. Li, J. Chen, Q. Luo, S. E. Grasby, T. Zhang, S. Yuan, Y. Xu, S. C. Finney, L. Sun, Y. Shen, Major volcanic eruptions linked to the Late Ordovician mass extinction: Evidence from mercury enrichment and Hg isotopes. *Glob. Planet. Change* **196**, 103374 (2021).
44. J. A. Yager, A. J. West, A. M. Thibodeau, F. A. Corsetti, M. Rigo, W. M. Berelson, D. J. Bottjer, S. E. Greene, Y. Ibarra, F. Jadoul, K. A. Ritterbush, N. Rollins, S. Rosas, P. D. Stefano, D. Sulca, S. Todaro, P. Wynn, L. Zimmermann, B. A. Bergquist, Mercury contents and isotope ratios from diverse depositional environments across the Triassic-Jurassic Boundary: Towards a more robust mercury proxy for large igneous province magmatism. *Earth Sci. Rev.* **223**, 103775 (2021).
45. J. Shen, J. Chen, T. J. Algeo, S. Yuan, Q. Feng, J. Yu, L. Zhou, B. O'Connell, N. J. Planavsky, Evidence for a prolonged Permian–Triassic extinction interval from global marine mercury records. *Nat. Commun.* **10**, 1563 (2019).
46. W. Zheng, A. Zhou, R. Sun, J. Chen, Mercury isotopes in sedimentary rocks as a paleoenvironmental proxy. *Chin. Sci. Bull.* **68**, 628–643 (2023).
47. S. J. Washburn, J. D. Blum, L. C. Motta, B. A. Bergquist, P. Weiss-Penzias, Isotopic composition of Hg in fogwaters of Coastal California. *Environ. Sci. Technol. Lett.* **8**, 3–8 (2021).
48. H. M. Amos, D. J. Jacob, D. G. Streets, E. M. Sunderland, Legacy impacts of all-time anthropogenic emissions on the global mercury cycle. *Global Biogeochem. Cycles* **27**, 410–421 (2013).
49. H. M. Horowitz, D. J. Jacob, Y. Zhang, T. S. Dibble, F. Slemr, H. M. Amos, J. A. Schmidt, E. S. Corbitt, E. A. Marais, E. M. Sunderland, A new mechanism for atmospheric mercury redox chemistry: Implications for the global mercury budget. *Atmos. Chem. Phys.* **17**, 6353–6371 (2017).
50. M. Jiskra, L.-E. Heimbürger-Boavida, M.-M. Desgranges, M. V. Petrova, A. Dufour, B. Ferreira-Araujo, J. Masbou, J. Chmeleff, M. Thyssen, D. Point, J. E. Sonke, Mercury stable isotopes constrain atmospheric sources to the ocean. *Nature* **597**, 678–682 (2021).
51. UN-Environment, Global Mercury Assessment 2018, (UN Environment Programme, Chemicals and Health Branch Geneva, Switzerland, 2019).
52. R. Sun, D. G. Streets, H. M. Horowitz, H. M. Amos, G. Liu, V. Perrot, J. P. Toutain, H. Hintelmann, E. M. Sunderland, J. E. Sonke, Historical (1850–2010) mercury stable isotope inventory from anthropogenic sources to the atmosphere. *Elem. Sci. Anth.* **4**, 000091 (2016).
53. P. Huybers, C. Langmuir, Feedback between deglaciation, volcanism, and atmospheric CO_2. *Earth Planet. Sci. Lett.* **286**, 479–491 (2009).
54. J. Du, A. C. Mix, B. A. Haley, C. L. Belanger, Volcanic trigger of ocean deoxygenation during Cordilleran ice sheet retreat. *Nature* **611**, 74–80 (2022).
55. F. Zhang, X. Zhu, B. Yan, B. Kendall, X. Peng, J. Li, T. J. Algeo, S. Romaniello, Oxygenation of a Cryogenian ocean (Nanhua Basin, South China) revealed by pyrite Fe isotope compositions. *Earth Planet. Sci. Lett.* **429**, 11–19 (2015).
56. P. B. Kelemen, C. E. Manning, Reevaluating carbon fluxes in subduction zones, what goes down, mostly comes up. *Proc. Natl. Acad. Sci. U.S.A.* **112**, E3997–E4006 (2015).
57. J. Farquhar, H. Bao, M. H. Thiemens, Atmospheric influence of Earth's earliest sulfur cycle. *Science* **289**, 756–758 (2000).
58. J. Farquhar, J. Savarino, S. Airieau, M. H. Thiemens, Observation of wavelength-sensitive mass-independent sulfur isotope effects during SO_2 photolysis: Implications for the early atmosphere. *J. Geophys. Res.* **106**, 32829–32839 (2001).
59. M. H. Thiemens, History and applications of mass-independent isotope effects. *Annual. Rev. Earth Planet. Sci.* **34**, 217–262 (2006).
60. M. H. Thiemens, M. Lin, Use of isotope effects to understand the present and past of the atmosphere and climate and track the origin of life. *Angewandte Chemie.* **58**, 6826–6844 (2019).
61. H. Oduro, B. Harms, H. O. Sintim, A. J. Kaufman, G. Cody, J. Farquhar, Evidence of magnetic isotope effects during thermochemical sulfate reduction. *Proc. Natl. Acad. Sci. U.S.A.* **108**, 17635–17638 (2011).
62. D. T. Johnston, J. Farquhar, D. E. Canfield, Sulfur isotope insights into microbial sulfate reduction: When microbes meet models. *Geochim. Cosmochim. Acta* **71**, 3929–3947 (2007).
63. J. Farquhar, D. T. Johnston, B. A. Wing, K. S. Habicht, D. E. Canfield, S. Airieau, M. H. Thiemens, Multiple sulphur isotopic interpretations of biosynthetic pathways: Implications for biological signatures in the sulphur isotope record. *Geobiology* **1**, 27–36 (2003).
64. D. T. Johnston, B. A. Wing, J. Farquhar, A. J. Kaufman, H. Strauss, T. W. Lyons, L. C. Kah, D. E. Canfield, Active microbial sulfur disproportionation in the Mesoproterozoic. *Science* **310**, 1477–1479 (2005).
65. S. Ono, B. A. Wing, D. T. Johnston, J. Farquhar, D. Rumble, Mass-dependent fractionation of quadruple stable sulfur isotope system as a new tracer of sulfur biogeochemical cycles. *Geochim. Cosmochim. Acta* **70**, 2238–2252 (2006).
66. Y. Shen, J. Farquhar, H. Zhang, A. Masterson, T. Zhang, B. A. Wing, Multiple S-isotopic evidence for episodic shoaling of anoxic water during Late Permian mass extinction. *Nat. Commun.* **2**, 210 (2011).
67. B. A. Wing, I. Halevy, Intracellular metabolite levels shape sulfur isotope fractionation during microbial sulfate respiration. *Proc. Natl. Acad. Sci. U.S.A.* **111**, 18116–18125 (2014).
68. A. Pellerin, T. H. Bui, M. Rough, A. Mucci, D. E. Canfield, B. A. Wing, Mass-dependent sulfur isotope fractionation during reoxidative sulfur cycling: A case study from Mangrove Lake, Bermuda. *Geochim. Cosmochim. Acta* **149**, 152–164 (2015).
69. K. Siedenberg, H. Strauss, R. Littke, Multiple sulfur isotopes ($\delta^{34}S$, $\Delta^{33}S$) and trace elements (Mo, U, V) reveal changing palaeoenvironments in the mid-Carboniferous Chokier Formation, Belgium. *Chem. Geol.* **441**, 47–62 (2016, 2016).
70. C. Thomazo, A. Brayard, S. Elmeknassi, E. Vennin, N. Olivier, G. Caravaca, G. Escarguel, E. Fara, K. G. Bylund, J. F. Jenks, D. A. Stephen, B. Killingsworth, P. Sansjofre, P. Cartigny, Multiple sulfur isotope signals associated with the late Smithian event and the Smithian/Spathian boundary. *Earth Sci. Rev.* **195**, 96–113 (2019).
71. P. W. Crockford, M. Kunzmann, A. Bekker, J. Hayles, H. Bao, G. P. Halverson, Y. Peng, T. H. Bui, G. M. Cox, T. M. Gibson, S. Wörndle, R. Rainbird, A. Lepland, N. L. Swanson-Hysell, S. Master,

B. Sreenivas, A. Kuznetsov, V. Krupenik, B. A. Wing, Claypool continued: Extending the isotopic record of sedimentary sulfate. *Chem. Geol.* **513**, 200–225 (2019).
72. P. Cadeau, P. Cartigny, C. Thomazo, D. Jezequel, C. Leboulanger, G. Sarazin, M. Ader, The Dziani Dzaha Lake: A long-awaited modern analogue for superheavy pyrites. *Geobiology* **20**, 444–461 (2022).
73. C. Cai, T. W. Lyons, P. Sun, D. Liu, D. Wang, C. J. Tino, G. Luo, Y. Peng, L. Jiang, Enigmatic super-heavy pyrite formation: Novel mechanistic insights from the aftermath of the Sturtian Snowball Earth. *Geochim. Cosmochim. Acta* **334**, 65–82 (2022).
74. B. Brunner, S. M. Bernasconi, A revised isotope fractionation model for dissimilatory sulfate reduction in sulfate reducing bacteria. *Geochim. Cosmochim. Acta* **69**, 4759–4771 (2005).
75. J. Farquhar, D. T. Johnston, B. A. Wing, Implications of conservation of mass effects on mass-dependent isotope fractionations: Influence of network structure on sulfur isotope phase space of dissimilatory sulfate reduction. *Geochim. Cosmochim. Acta* **71**, 5862–5875 (2007).
76. G. Zhang, X. Zhang, D. Hu, D. Li, T. J. Algeo, J. Farquhar, C. M. Henderson, L. Qin, M. Shen, D. Shen, S. D. Schoepfer, K. Chen, Y. Shen, Redox chemistry changes in the Panthalassic Ocean linked to the end-Permian mass extinction and delayed Early Triassic biotic recovery. *Proc. Natl. Acad. Sci. U.S.A.* **14**, 1806–1810 (2017).
77. C. Scott, B. A. Wing, A. Bekker, N. J. Planavsky, P. Medvedev, S. M. Bates, M. Yun, T. W. Lyons, Pyrite multiple-sulfur isotope evidence for rapid expansion and contraction of the early Paleoproterozoic seawater sulfate reservoir. *Earth Planet. Sci. Lett.* **389**, 95–104 (2014).
78. W. D. Leavitt, I. Halevy, A. S. Bradley, D. T. Johnston, Influence of sulfate reduction rates on the Phanerozoic sulfur isotope record. *Proc. Natl. Acad. Sci. U.S.A.* **110**, 11244–11249 (2013).
79. A. Robock, Volcanic eruptions and climate. *Rev. Geophys.* **38**, 191–219 (2000).
80. M. Baroni, M. H. Thiemens, R. J. Delmas, J. Savarino, Mass-independent sulfur isotopic compositions in stratospheric volcanic eruptions. *Science* **315**, 84–87 (2007).
81. E. Gautier, J. Savarino, J. Hoek, J. Erbland, N. Caillon, S. Hattori, N. Yoshida, E. Albalat, F. Albarede, J. Farquhar, 2600-years of stratospheric volcanism through sulfate isotopes. *Nat. Commun.* **10**, 466 (2019).
82. D. Hu, M. Li, X. Zhang, A. V. Turchyn, Y. Gong, Y. Shen, Large mass-independent sulphur isotope anomalies link stratospheric volcanism to the Late Ordovician mass extinction. *Nat. Commun.* **11**, 2297 (2020).
83. S. Kremser, L. W. Thomason, M. von Hobe, M. Hermann, T. Deshler, C. Timmreck, M. Toohey, A. Stenke, J. P. Schwarz, R. Weigel, S. Fueglistaler, F. J. Prata, J.-P. Vernier, H. Schlager, J. E. Barnes, J.-C. Antuna-Marrero, D. Fairlie, M. Palm, E. Mahieu, J. Notholt, M. Rex, C. Bingen, F. Vanhellemont, A. Bourassa, J. M. C. Plane, D. Klocke, S. A. Carn, L. Clarisse, T. Trickl, R. Neely, A. D. James, L. Rieger, J. C. Wilson, B. Meland, Stratospheric aerosol-observations, processes, and impact on climate. *Rev. Geophys.* **54**, 278–335 (2016).
84. K. Zhao, X. Lang, G. Zhu, M. Feng, R. He, C. Guan, S. Li, S. Zhu, C. Zhou, Low marine sulfate levels during the initiation of the Cryogenian Marinoan glaciation. *Precambrian Res.* **377**, 106737 (2022).
85. Q. Huang, Y. Liu, J. Chen, X. Feng, W. Huang, S. Yuan, H. Cai, X. Fu, An improved dual-stage protocol to pre-concentrate mercury from airborne particles for precise isotopic measurement. *J. Anal. At. Spectrom* **30**, 957–966 (2015).
86. J. R. Hulston, H. G. Thode, Variations in the S33, S34, and S36 contents of meteorites and their relation to chemical and nuclear effects. *J. Geophys. Res.* **7**, 3475–3484 (1965).
87. J. Farquhar, B. A. Wing, Multiple sulfur isotopes and the evolution of the atmosphere. *Earth Planet. Sci. Lett.* **213**, 1–13 (2003).
88. M. L. Gomes, M. T. Hurtgen, Sulfur isotope systematics of a euxinic, low-sulfate lake: Evaluating the importance of the reservoir effect in modern and ancient oceans. *Geology* **41**, 663–666 (2013).

Acknowledgments: We thank P. F. Hoffman and B. A. Wing for constructive comments that have greatly improved our study and X. Lang for discussions. **Funding:** This study was supported by National Natural Science Foundation of China (41721002, 41890842, 41830647, and 42103074), National Postdoctoral Program for Innovative Talents of China (BX2021278), and 111 project (B14026). **Author contributions:** M.L. designed the project; M.L., Y.X., X.Z., F.A.M., Y.F., and Y.S. conducted field work, stratigraphic analyses, and sampling; M.L., Y.X., L.S., X.Z., J.F., and Y.S. carried out sulfur isotopic analyses; J.C., K.Z., and M.L. conducted Hg isotopic analyses; M.L., D.L., and R.S. conducted sulfur and Hg cycle modeling; M.L. wrote the paper with inputs from all co-authors. **Competing interests:** The authors declare that they have no competing interests. **Data and materials availability:** All data needed to evaluate the conclusions in the paper are present in the paper and/or the Supplementary Materials.

Submitted 24 March 2023
Accepted 2 August 2023
Published 6 September 2023
10.1126/sciadv.adh9502